Gust Buffeting and Aerodynamic Admittance of Structures with Arbitrary Mode Shapes. II: A POD-Based Interpretation

Giovanni Solari, M.ASCE[1]; and Patricia Martín[2]

Abstract: Studies carried out on gust buffeting and aerodynamic admittance show that mode shape represents a sort of watershed. If the mode does not change sign along the structure axis, the problem admits a robust conceptual interpretation based on energy cascade and a simple closed-form solution. If, instead, the mode changes sign, the solution calls for numerical tools, and its physical interpretation definitely is unclear. The companion paper investigated this issue within the novel framework of the enhanced equivalent spectrum technique and derived a closed-form solution of the aerodynamic admittance that can be applied to any mode using quasi-steady theory. This solution is precise and simple for modes with a few changes of sign, but it becomes laborious with increasing mode shape complexity; in addition, it provides a partial conceptual interpretation. Both these limitations were overcome in this paper, in which the application of proper orthogonal decomposition led to a full conceptual interpretation of aerodynamic admittance and to a simple and general closed-form solution. Analyses were limited here to single modes; multiple arbitrary modes are left for future research, as is the generalization of these concepts to arbitrary influence functions. **DOI: 10.1061/(ASCE)EM.1943-7889.0001873.**

Author keywords: Aerodynamic admittance; Buffeting; Double modal transformation; Energy cascade; Mode shape; Proper orthogonal decomposition; Wind loading; Wind mode.

Introduction

Studies of gust buffeting (Solari 2019) have pointed out the focal role of the mode shape with reference to aerodynamic admittance and, in particular, to the circumstance according to which the mode changes or does not change sign along the structural axis. In this framework, Davenport (1977) and Hansen and Krenk (1999) classified mode shapes into three families, called by Solari and Martín (2020) Type A, B, and C modes.

Type A modes do not change sign; accordingly, aerodynamic admittance is one at the zero frequency and decreases as frequency increases. Type B modes mainly are skew-symmetric; the aerodynamic admittance is null at the zero frequency, grows as this quantity increases, reaches a relative maximum, and then decreases. Type C modes have intermediate shapes and lead to intermediate trends.

The analyses reported subsequently focused on slender structures, were based on quasi-steady theory, and neglected as usual the imaginary part of the turbulence cross-spectrum.

Based on these hypotheses, for modes that do not change sign (Type A modes), an energy cascade provides a robust physical interpretation according to which the maximum loading corresponds to large eddies with a low frequency content, and aerodynamic admittance decreases as the frequency of eddies and/or the length of the structure increase. For this situation, Piccardo and Solari (1998) provided a general closed-form expression (CFS).

In the case of modes that change sign (Types B and C), energy cascade alone cannot interpret the relative maximum of aerodynamic admittance due to its prerogative of representing turbulence at a single point, missing any information about the phase shift of eddies at distinct points. As a consequence, the expression of aerodynamic admittance calls for numeric solutions.

Solari and Martín (2020) studied this issue in the framework of the enhanced equivalent spectrum technique, a method that extends to any mode shape the generalized equivalent spectrum technique (Piccardo and Solari 1998), which is limited to fundamental regular modes that do not change sign. Using this method, the link between aerodynamic admittance and mode shape is evaluated by dividing the structural domain into subdomains in which piecewise modes are regular and do not change sign. This allows solving the problem through the application of classical methods to each subdomain. This solution provides a partial conceptual interpretation; in addition, it is precise and simple for modes with a few changes of sign. However, it becomes laborious to apply with increasing mode shape complexity.

Both these limitations were overcome in this paper through the joint application of proper orthogonal decomposition (POD) (Solari et al. 2007; Carassale et al. 2007) and double modal transformation (DMT) (Carassale et al. 2001). This approach leads to a full physical interpretation and a simple and general CFS of aerodynamic admittance.

After this brief introduction, this paper summarizes the fundamentals of the enhanced equivalent spectrum technique (Solari and Martín 2020) and the bases of POD in terms of its application to aerodynamic admittance. Then it studies the role of structural modes with regard to the shape of aerodynamic admittance, refines the interpretation of this quantity by making recourse to effective turbulence (Tubino and Solari 2007), and introduces a simple and

[1]Professor, Dept. of Civil, Chemical, and Environmental Engineering (DICCA), Polytechnic School, Univ. of Genova, Via Montallegro, 1, Genova 16145, Italy (corresponding author). ORCID: https://orcid.org/0000-0002-2376-4498. Email: giovanni.solari@unige.it

[2]Associate Professor, Dept. of Structures, Technological Univ. of Havana José Antonio Echeverría (CUJAE), Havana 19390, Cuba.

Note. This manuscript was submitted on February 19, 2020; approved on August 3, 2020; published online on November 11, 2020. Discussion period open until April 11, 2021; separate discussions must be submitted for individual papers. This paper is part of the ***Journal of Engineering Mechanics***, © ASCE, ISSN 0733-9399.

general CFS of the aerodynamic admittance of structures with arbitrary modes. Two applications studied by Solari and Martín (2020) are examined to highlight the potential of the new solution. Finally, the main results are summarized and the prospects of this research are discussed.

Fundamentals

This section provides the fundamentals of the gust buffeting and aerodynamic admittance of structures with arbitrary modes. First, it summarizes the enhanced equivalent spectrum technique. Then, it reviews the bases of POD and derives a novel expression of aerodynamic admittance.

Enhanced Equivalent Spectrum Technique

Consider a structure whose length l is much greater than the reference size b of its cross section. Referring to Fig. 1 of Solari and Martín (2020), x, y, z is a Cartesian system with origin at o; z coincides with the structural axis, x is aligned with the mean wind direction, and o lies at the height H above ground. Furthermore, X, Y, Z is a Cartesian system with origin at O; the X, Y-plane is coplanar with the ground; the Y, Z-plane is coplanar with the y, z-plane; X is parallel to x; Z is directed upwards and passes through o; and z is rotated φ with respect to Z.

The wind loading $f_\alpha(z,t) = \bar{f}_\alpha(z) + f'_\alpha(z,t)$ is a stationary Gaussian field, where $\alpha = x, y, \theta$; t is time; f_x, f_y, and f_θ are alongwind and crosswind force and torsional moment around z per unit length; and $\bar{f}_\alpha$ and f'_α are the mean value and the fluctuation of f_α.

The structure has linear elastic behavior with viscous damping and three uncoupled components of motion: the alongwind and crosswind displacement, x and y; and the torsional rotation θ around axis z. Each $\alpha = x, y, \theta$ motion component is a stationary Gaussian process defined as $\alpha(r,t) = \bar{\alpha}(r) + \alpha'(r,t)$, where $0 \le r \le l$, and $\bar{\alpha}$ and α' are mean value and fluctuation of α. Solari and Martín (2020) provided the expressions of the parameters needed to determine the dynamic response for any mode k.

The power spectral density (PSD) of the kth modal loading in the α direction is given by

$$S_{f\alpha k}(n) = l^2 \int_0^1 \int_0^1 S_{f\alpha}(\zeta,\zeta';n)\psi_{\alpha k}(\zeta)\psi_{\alpha k}(\zeta')d\zeta d\zeta' \tag{1}$$

where n = frequency; $\zeta = z/l$ and $\zeta' = z'/l$ = nondimensional coordinates; $\psi_{\alpha k}$ = kth mode in α direction; and $S_{f\alpha k}$ = cross-PSD (CPSD) of f'_α, expressed as

$$S_{f\alpha}(\zeta,\zeta';n) = \sum_\varepsilon \bar{f}_{\alpha\varepsilon}(\zeta)\bar{f}_{\alpha\varepsilon}(\zeta')S^*_{\varepsilon\varepsilon}(\zeta,\zeta';n) \tag{2}$$

$$\bar{f}_{\alpha\varepsilon}(\zeta) = \frac{1}{2}\rho\bar{u}^2(\zeta)b\lambda_\alpha c_{\alpha\varepsilon}[I_\varepsilon(\zeta) + \delta_{\varepsilon u}] \tag{3}$$

$$S^*_{\varepsilon\varepsilon}(\zeta,\zeta';n) = \sqrt{S^*_\varepsilon(\zeta;n)S^*_\varepsilon(\zeta';n)}\,\mathrm{Coh}_{\varepsilon\varepsilon}(\zeta,\zeta';n) \tag{4}$$

where Σ_ε = sum of three fluctuating loading terms with indices $\varepsilon = u, v$, and w, related to the turbulence components u', v', and w'; ρ = density of air; $\bar{u}$ = mean wind speed; $\lambda_x = \lambda_y = 1$; $\lambda_\theta = b$; $\delta_{\varepsilon u}$ = Kronecker's delta; and $c_{\alpha\varepsilon} = \alpha$, εth element of 3×3 aerodynamic matrix

$$[c] = \begin{bmatrix} c_d & (c'_d - c_\ell)\cos\phi & (c'_d - c_\ell)\sin\phi \\ c_\ell & (c_d + c'_\ell)\cos\phi & (c_d + c'_\ell)\sin\phi \\ c_m & c'_m\cos\phi & c'_m\sin\phi \end{bmatrix} \tag{5}$$

where c_d, c_ℓ, and c_m = drag, lift, and torsional moment coefficients; c'_d, c'_ℓ, and c'_m = prime angular derivatives; $I_u = \sigma_u/\bar{u}$, $I_v = \sigma_v/\bar{u}$, and $I_w = \sigma_w/\bar{u}$ = turbulence intensities, where σ_u, σ_v, and σ_w = standard deviations of u', v', and w'; S^*_ε, $S^*_{\varepsilon\varepsilon}$, and $\mathrm{Coh}^*_{\varepsilon\varepsilon}$ = PSD, CPSD, and coherence function of $\varepsilon^* = u^*, v^*, w^*$, where $u^* = u'/\sigma_u$, $v^* = v'/\sigma_v$, and $w^* = w'/\sigma_w$ are reduced turbulence components. Adopting the model of Solari and Piccardo (2001)

$$S^*_\varepsilon(\zeta;n) = \frac{d_\varepsilon L_\varepsilon(\zeta)/\bar{u}(\zeta)}{[1 + 1.5nd_\varepsilon L_\varepsilon(\zeta)/\bar{u}(\zeta)]^{5/3}} \tag{6}$$

$$\mathrm{Coh}_{\varepsilon\varepsilon}(\zeta,\zeta';n) = \exp\left\{-\frac{2nc_\varepsilon|\zeta - \zeta'|}{\bar{u}(\zeta) + \bar{u}(\zeta')}\right\} \tag{7}$$

where $d_u = 6.868$; $d_v = d_w = 9.434$; L_ε = integral length scale; and c_ε = exponential decay coefficient. Eq. (6) may be replaced by any other expression. The use of Eq. (7) is functional to the subsequent developments.

The enhanced equivalent spectrum technique consists of replacing the actual turbulent field with an equivalent monovariate process, assuming $\mathrm{Coh}_{\varepsilon\varepsilon} = 1$ and replacing S^*_ε with

$$S^*_{\varepsilon,eq}(n) = S^*_\varepsilon(\bar{\zeta}_{\alpha k};n)\chi_{\alpha k\varepsilon}(n) \tag{8}$$

where $S^*_{\varepsilon,eq}$ = PSD of reduced equivalent turbulent fluctuation; $\bar{\zeta}_{\alpha k}$ = reference value of $\zeta_{\alpha k}$; and $\chi_{\alpha k\varepsilon}$ = frequency filter that plays the role of aerodynamic admittance

$$\chi_{\alpha k\varepsilon}(n) = \frac{1}{F^2_{\alpha k}}\int_0^1\int_0^1 \exp\{-\kappa_{\alpha k\varepsilon}(n)|\zeta - \zeta'|\}\psi_{\alpha k}(\zeta)\psi_{\alpha k}(\zeta')d\zeta d\zeta' \tag{9}$$

where $F_{\alpha k}$ = generalized participation coefficient; and $\kappa_{\alpha k\varepsilon}$ = reduced frequency

$$F_{\alpha k} = \int_0^1 |\psi_{\alpha k}(\zeta)|d\zeta \tag{10}$$

$$\kappa_{\alpha k\varepsilon}(n) = \frac{nc_\varepsilon l}{\bar{u}(\bar{\zeta}_{\alpha k})} \tag{11}$$

Accordingly, Eq. (1) may be rewritten as

$$S_{f\alpha k}(n) = l^2F^2_{\alpha k}\sum_\varepsilon \bar{f}^2_{\alpha\varepsilon}(\bar{\zeta}_{\alpha k})S^*_\varepsilon(\bar{\zeta}_{\alpha k};n)\chi_{\alpha k\varepsilon}(n) \tag{12}$$

Solari and Martín (2020) proved that

$$\chi_{\alpha k\varepsilon}(0) = \frac{1}{F^2_{\alpha k}}\left[\int_0^1 \psi_{\alpha k}(\zeta)d\zeta\right]^2 \tag{13}$$

whereas for n tending to infinity, the tail of Eq. (9) is given by

$$\chi_{\alpha k\varepsilon}(n) = \frac{1}{k^*_{\alpha k}\kappa_{\alpha k\varepsilon}(n)}; \qquad k^*_{\alpha k} = \frac{1}{2}\frac{F^2_{\alpha k}}{\int_0^1 \psi^2_{\alpha k}(\zeta)d\zeta} \tag{14}$$

Fig. 2 of Solari and Martín (2020) shows the rigorous solutions of Eqs. (9) and (10) provided by MATLAB version 2019a software for 17 noteworthy modes $\psi_{\alpha k}$ classified into three families, referred to as Types A, B, and C. It also provides $\chi_0 = \chi_{\alpha k\varepsilon}(0)$, the $\kappa_m = \kappa_{\alpha k\varepsilon}$ value for which $\chi_{\alpha k\varepsilon}$ is maximum; the relative maximum $\chi_{\max}$ of $\chi_{\alpha k\varepsilon}$; and the $k^* = k^*_{\alpha k}$ value defined by Eq. (14).

Proper Orthogonal Decomposition

Solari and Martín (2020) highlighted some noteworthy trends that, to authors' knowledge, never have been interpreted in an exhaustive way. They concern the growth of aerodynamic admittance $\chi_{\alpha k\varepsilon}$ with the reduced frequency $\kappa = \kappa_{\alpha k\varepsilon}$, the achievement of the relative maximum $\chi_{\max}$ for $\kappa = \kappa_m$, and its decrease as κ tends to infinity. In particular, κ_m increases with the increase of the number N of subdomains in which the piecewise mode $\psi_{\alpha k}$ has a constant sign. As N increases, $\chi_{\max}$ decreases; for Type C modes, χ_0 also decreases as N increases.

This behavior is explained only partially by energy cascades (Solari and Martín 2020) due to the limitation of describing the turbulence at a single point, and therefore lacking any information about the phase shift of its component eddies at different points. POD (Di Paola 1998; Tamura et al. 1999; Solari and Carassale 2000; Chen and Kareem 2005; Solari et al. 2007; Carassale et al. 2007) and DMT (Solari and Carassale 2000; Carassale et al. 2001; Tubino and Solari 2007) provide concepts and rules that contribute greatly to clarify the preceding trends.

Investigating the phase shift of eddies at different points highlights a potential problem, namely the use of a turbulence model [Eqs. (6) and (7)] neglecting the imaginary part of the CPSD, and therefore quad-coherence. According to ESDU (1991), this quantity is negligible for horizontal structures, but not for vertical structures. In this second case, however, ESDU states that quad-coherence can be neglected when the atmosphere is isotropic, i.e., in the inertial subrange and in the high-frequency range. Thus, quad-coherence is relevant only in the low-frequency range. Herein its importance may become relevant when the separation between two points is large, namely when one of them is high above ground level. In this case, however, turbulence is approaching isotropy and the role of quad-coherence again is questionable. In other words, the importance of quad-coherence is restricted to a limited range within which uncertainties are huge, as confirmed by field experiments (Mann 1994). For all these reasons, the authors highlight the importance of research in this field but herein follow the almost totality of researchers who used a real turbulence CPSD to investigate gust buffeting.

Let $\gamma_{j\varepsilon}(n)$ and $\theta_{j\varepsilon}(\zeta, n)(j = 1, 2, \cdots)$ be the eigenvalues and eigenfunctions of the CPSD of the reduced turbulence component ε^* [Eq. (4)]. They are the nontrivial solutions of the Fredholm integral equation of the second type (Carassale and Solari 2002)

$$\theta_{j\varepsilon}(\zeta, n) = \frac{1}{\gamma_{j\varepsilon}(n)} \int_0^1 S^*_{\varepsilon\varepsilon}(\zeta, \zeta'; n)\theta_{j\varepsilon}(\zeta', n)d\zeta' \tag{15}$$

Because $S^*_{\varepsilon\varepsilon}$ is bounded, real [Eqs. (4) and (7)], and nonnegative definite, its eigenvalues are real and nonnegative; in addition, its eigenfunctions are real and can be made orthonormal as

$$\int_0^1 \theta_{i\varepsilon}(\zeta, n)\theta_{j\varepsilon}(\zeta, n)d\zeta = \delta_{ij} \tag{16}$$

$$\int_0^1 \int_0^1 S^*_{\varepsilon\varepsilon}(\zeta, \zeta'; n)\theta_{i\varepsilon}(\zeta, n)\theta_{j\varepsilon}(\zeta', n)d\zeta d\zeta' = \gamma_{j\varepsilon}(n)\delta_{ij} \tag{17}$$

The completeness of the set of the eigenfunctions enables the spectral decomposition

$$S^*_{\varepsilon\varepsilon}(\zeta, \zeta', n) = \sum_j \theta_{j\varepsilon}(\zeta, n)\theta_{j\varepsilon}(\zeta', n)\gamma_{j\varepsilon}(n) \tag{18}$$

In the case of infinite eigenvalues, the sum in Eq. (18) has infinite terms; however, sorting the eigenvalues in decreasing order, it can be truncated, retaining a finite number of significant terms.

Assuming that turbulence PSD may be evaluated for $\zeta = \bar{\zeta} = \bar{\zeta}_{\alpha k}$ and substituting Eqs. (7) and (11) into Eq. (15), the eigenvalue problem assumes the form

$$\theta_{j\varepsilon}(\zeta, n) = \frac{1}{\tilde{\gamma}_{j\varepsilon}(n)} \int_0^1 \exp\{-\kappa_{\alpha k\varepsilon}(n)|\zeta - \zeta'|\}\theta_{j\varepsilon}(\zeta', n)d\zeta' \tag{19}$$

where

$$\tilde{\gamma}_{j\varepsilon}(n) = \frac{\gamma_{j\varepsilon}(n)}{S^*_{\varepsilon}(\bar{\zeta}; n)} \tag{20}$$

is the reduced eigenvalue; it depends on n through $\kappa = \kappa_{\alpha k\varepsilon}(n)$ (Carassale and Solari 2002).

Fig. 1 shows the analytical (solid lines) and numerical (dashed lines) solutions of the reduced eigenvalues and eigenfunctions (Carassale and Solari 2002). Fig. 1(a) highlights the similarity between the reduced eigenvalues and the aerodynamic admittances related to Type A and B modes. The largest detachment caused by the analytical solution concerns the first wind mode (Carassale and Solari 2002) for $\kappa < 0.1$ (shaded area). The eigenfunctions [Fig. 1(b)] represent waves or elementary shapes, also called wind modes (Di Paola 1998), which are perfectly coherent along the structural axis and perfectly incoherent with each other (Li and Kareem 1995). The change of sign of the wind modes along ζ corresponds to counter-phase turbulence coherent structures that energy cascade alone is not able to grasp.

The preceding formulation lends itself to noteworthy conceptual, physical, and engineering interpretations by expanding the turbulence component ε^* into a series of eigenfunctions, the wind modes, weighted by independent time-histories the PSDs of which are the wind eigenvalues. In other words, eigenfunctions define elementary shapes of the wind loading, whereas eigenvalues specify their power content. Substituting this series expansion into structural modal analysis originates DMT (Solari and Carassale 2000; Carassale et al. 2001), in which a parameter of great expressiveness arises, the cross-modal participation coefficient is

$$A_{\alpha kj\varepsilon}(n) = \int_0^1 \psi_{\alpha k}(\zeta)\bar{f}_{\alpha\varepsilon}(\zeta)\theta_{j\varepsilon}(\zeta, n)d\zeta \quad (j = 1, 2, \cdots; k = 1, 2, \cdots) \tag{21}$$

where $A_{\alpha kj\varepsilon}$ = influence of jth wind mode (associated with ε turbulence component) on kth structural mode in α direction. Using modal truncation, only a subset of wind modes excites a subset of structural modes. In addition, due to the reciprocal shape of wind and structural modes, several cross-modal participation coefficients often are negligible; in this case, the jth wind mode is said to be quasi-orthogonal to the kth structural mode with respect to $\bar{f}_{\alpha\varepsilon}$. Thus, only a limited subset of wind modes usually excites a limited subset of structure modes. Furthermore, in some cases, the similar shape of wind and structural modes makes the cross-modal participation coefficients with equal indexes much greater than others; in this case, each wind mode mostly excites the sole corresponding structural mode.

Now, substitute Eqs. (4), (7), (11), and (20) into Eq. (18). Delete the term S^*_{ε} that appears in both the left-hand and right-hand members. It follows that

$$\mathrm{Coh}_{\varepsilon\varepsilon}(\zeta, \zeta'; n) = \exp\{-\kappa_{\alpha k\varepsilon}(n)|\zeta - \zeta'|\} = \sum_j \theta_{j\varepsilon}(\zeta, n)\theta_{j\varepsilon}(\zeta', n)\tilde{\gamma}_{j\varepsilon}(n) \tag{22}$$

Finally, substitute Eqs. (11) and (22) into Eq. (9). It follows that aerodynamic admittance can be expanded into the following series of the reduced wind eigenvalues:

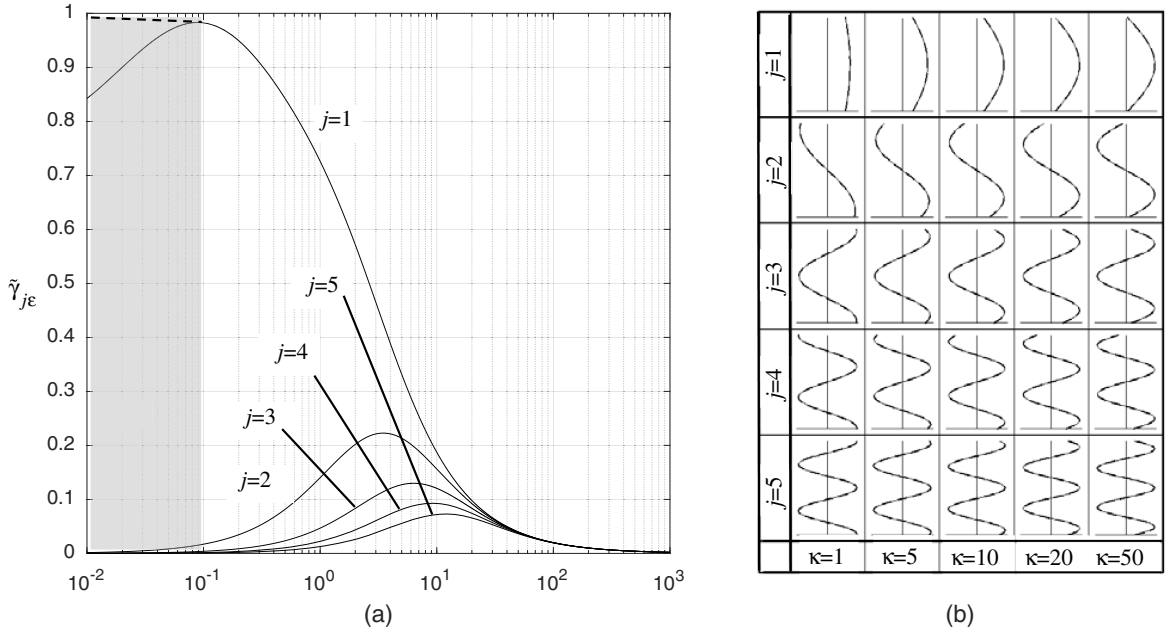

Fig. 1. (a) Reduced eigenvalues [Eq. (20)]; and (b) eigenfunctions [Eq. (19)].

$$\chi_{\alpha k\varepsilon}(n) = \frac{1}{F_{\alpha k}^2}\sum_j \left[\int_0^1 \theta_{j\varepsilon}(\zeta;n)\psi_{\alpha k}(\zeta)d\zeta\right]^2 \tilde{\gamma}_{j\varepsilon}(n) \tag{23}$$

In particular, unlike Eq. (9), which involves the solution of a double integral, Eq. (23) provides a novel expression of aerodynamic admittance by a single integral. Moreover, it establishes the link among aerodynamic admittance, structural mode, and reduced wind eigenvalues and eigenfunctions. The weight of individual wind eigenvalues depends on the reciprocal shape of structural and wind modes, similarly to double modal transformation, in which Eq. (21) includes the term $\bar{f}_{\alpha\varepsilon}$ missing in Eq. (23). Similarly, Eq. (23) can be simplified when most wind modes are orthogonal or quasi-orthogonal to the kth structural mode; in this case, Eq. (23) reduces itself to a linear combination of a few wind eigenvalues. Furthermore, in some particular cases only one mode, usually the mode with index $j = k$, contributes to reconstruct aerodynamic admittance; in this case, $\chi_{\alpha k\varepsilon}$ tends to reproduce the shape of the pertinent wind eigenvalue.

Interpretations and Solutions

This section applies the expressions obtained previously with the aim of interpreting the shape of aerodynamic admittance with reference to structural modes, refines this interpretation by making recourse to effective turbulence, and proposes a simple and general CFS of the aerodynamic admittance of structures with arbitrary modes.

POD- and DMT-Based Interpretation of Aerodynamic Admittance

This section examines aerodynamic admittance for some noteworthy structural modes and interprets its physical meaning based on cross-modal participation coefficients [Eq. (21)] and the expansion through a series of wind modes [Eq. (23)]. It also provides some preliminary expressions of the parameters needed to construct a CFS.

Sinusoidal Structural Modes

Sinusoidal structural modes exhibit similar trends to wind modes [Fig. 1(b)]. Accordingly, they have orthogonality or quasi-orthogonality properties that make the physical interpretation of aerodynamic admittance maximally expressive. Consider the structural modes

$$\psi_{\alpha k}(\zeta) = g(\zeta) = \sin(i\pi\zeta) \quad (i = 1, 2, \cdots) \tag{24}$$

where $i = 1$ denotes a symmetric Type A mode [Mode 2 in Fig. 2 of Solari and Martín (2020)]; $i = 2$ (Mode 6), $i = 4$ (Mode 10), $i = 6$ (Mode 11), and $i = 8$ (Mode 12) denote skew-symmetric Type B modes; and $i = 3$ (Mode 15), $i = 5$ (Mode 16), and $i = 7$ (Mode 17) denote symmetric intermediate Type C modes.

Fig. 2 shows the cross-modal participation coefficients [Eq. (21)] for $\bar{f}_{\alpha\varepsilon} = 1$. Due to the similarity between modes with the same index, they are large for $j = i$, and small for $j \neq i$. This means that structure and wind modes with different indexes are quasi-orthogonal to each other, and the kth structure mode is excited mainly by the sole $j = i$th wind mode. This is almost rigorous for even i values over the whole frequency range and in any case for large values of the reduced frequency κ. In contrast, in the low-frequency range, structure modes with odd indices i also are excited partially by wind modes with indices $j \neq i$.

To better clarify this issue, Fig. 3 shows the aerodynamic admittance $\chi_{\alpha k\varepsilon}$ [Eq. (9)] related to the three structural modes with indices $i = 1, 2, 3$. Solid lines correspond to $\chi_{\alpha k\varepsilon}$ reconstructed by the series expansion of the wind modes [Eq. (23)] given in closed form. Dashed lines refer to the rigorous expression of $\chi_{\alpha k\varepsilon}$ [Eq. (9)].

Fig. 3(a) shows $\chi_{\alpha k\varepsilon}$ for the structure mode with $i = 1$. The sole wind mode with $j = i = 1$ is enough to reconstruct $\chi_{\alpha k\varepsilon}$ on the whole frequency range. Its shape thus corresponds to the first reduced wind eigenvalue [Fig. 1(a)]. It is one for $\kappa = 0$ and decreases as κ increases; thus, its power is maximum at the zero frequency and its harmonic content is concentrated in the low-frequency range. This gives rise to a unit aerodynamic admittance for $\kappa = 0$ that decreases as κ increases.

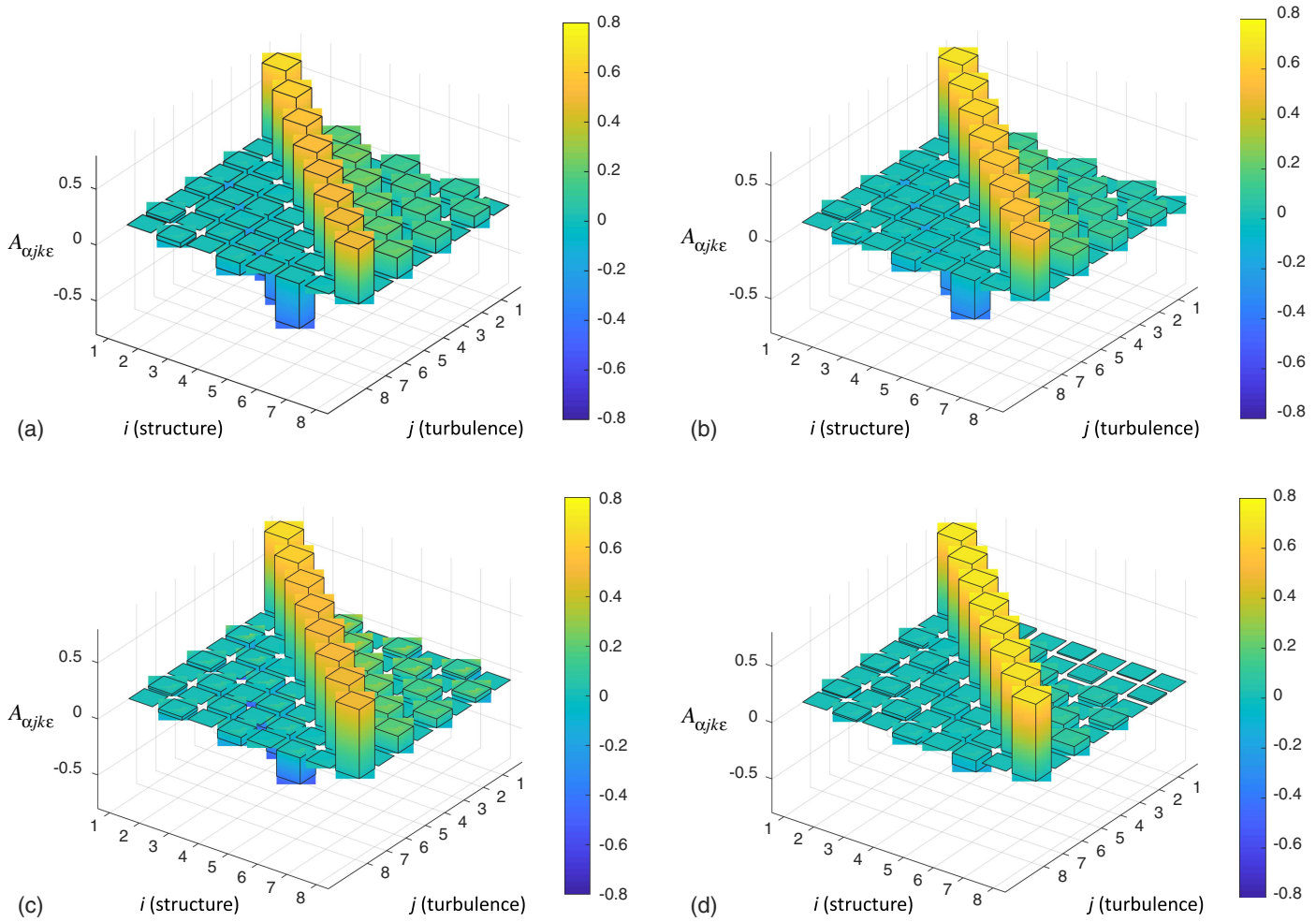

Fig. 2. Cross-modal participation coefficients for structure mode in Eq. (24) ($i, j = 1, 2, \ldots, 8$) for (a) $\kappa = 1$; (b) $\kappa = 5$; (c) $\kappa = 15$; and (d) $\kappa = 50$.

Fig. 3(b) shows $\chi_{\alpha k\varepsilon}$ for the structural mode with $i = 2$. The wind modes with odd indices j are orthogonal to it and do not provide any contribution; the wind mode with index $j = 4$ and the upper even modes provide limited contributions. Thus, the sole wind mode with $j = i = 2$ is enough to reconstruct $\chi_{\alpha k\varepsilon}$ on the whole frequency range, and its shape corresponds to the second reduced wind eigenvalue [Fig. 1(a)]. It is null for $\kappa = 0$; increases as κ increases; reaches its maximum at $\kappa = \kappa_m$, which corresponds to the maximum power of the wind mode; and then decreases.

Results not shown here prove that this principle can be generalized to all structural modes with even i values. In this case, the sole wind mode $j = i$ is enough to reconstruct $\chi_{\alpha k\varepsilon}$, and its shape corresponds almost perfectly to the $j = i$th reduced wind eigenvalue. Hence $\kappa = \kappa_m$ increases as i increases whereas $\chi_{\max}$ decreases [Fig. 1(a)].

Fig. 3(c) shows $\chi_{\alpha k\varepsilon}$ for the structural mode with $i = 3$. It requires taking into account both the wind mode with index $j = 1$, which is related to the low-frequency range, and the wind mode with index $j = 3$, which is related to the reduced frequency domain centered around $\kappa = \kappa_m$. The shape of $\chi_{\alpha k\varepsilon}$ thus corresponds to a combination of the first and third reduced wind eigenvalues, as shown partially by Fig. 2. This explains the trend of aerodynamic admittance: it takes a value between 0 and 1 for $\kappa = 0$; increases as κ increases; reaches its maximum at $\kappa = \kappa_m$; which corresponds to the maximum power of the wind mode with index $j = 3$; and then decreases. Furthermore, wind modes with even indices j are orthogonal to the structural mode and do not provide any contribution; the wind mode with index $j = 5$ and upper odd modes provide limited contributions.

Results not shown here prove that this principle can be generalized to all structural modes with odd i values greater than 1. In this case, the reconstruction of $\chi_{\alpha k\varepsilon}$ takes into account both the wind modes with indexes $j = 1$ and $j = i$. The shape of $\chi_{\alpha k\varepsilon}$ thus corresponds to a combination of the first and $j = i$th reduced wind eigenvalues. Hence $\kappa = \kappa_m$ increases as i increases, whereas both χ_0 and $\chi_{\max}$ decrease [Fig. 1(a)].

Structural Mode 14

Consider the Type C intermediate Mode 14 [Fig. 2 of Solari and Martín (2020)]

$$\psi_{\alpha k}(\zeta) = -5.5\zeta^2 + 8\zeta^3 - 1.5\zeta^4 \tag{25}$$

The comparison of its shape with that of wind modes in Fig. 1(b) exhibits great diversity because the portions of the structural mode with constant sign have different shapes and lengths. Therefore, no quasi-orthogonality property occurs, and this makes the physical interpretation of aerodynamic admittance more complex than in the case of structural sinusoidal modes.

Fig. 4 shows the cross-modal participation coefficients [Eq. (21)] for $\bar{f}_{\alpha\varepsilon} = 1$. They tend to decrease as j increases, but none is clearly negligible. In addition, all cross-modal participation coefficients

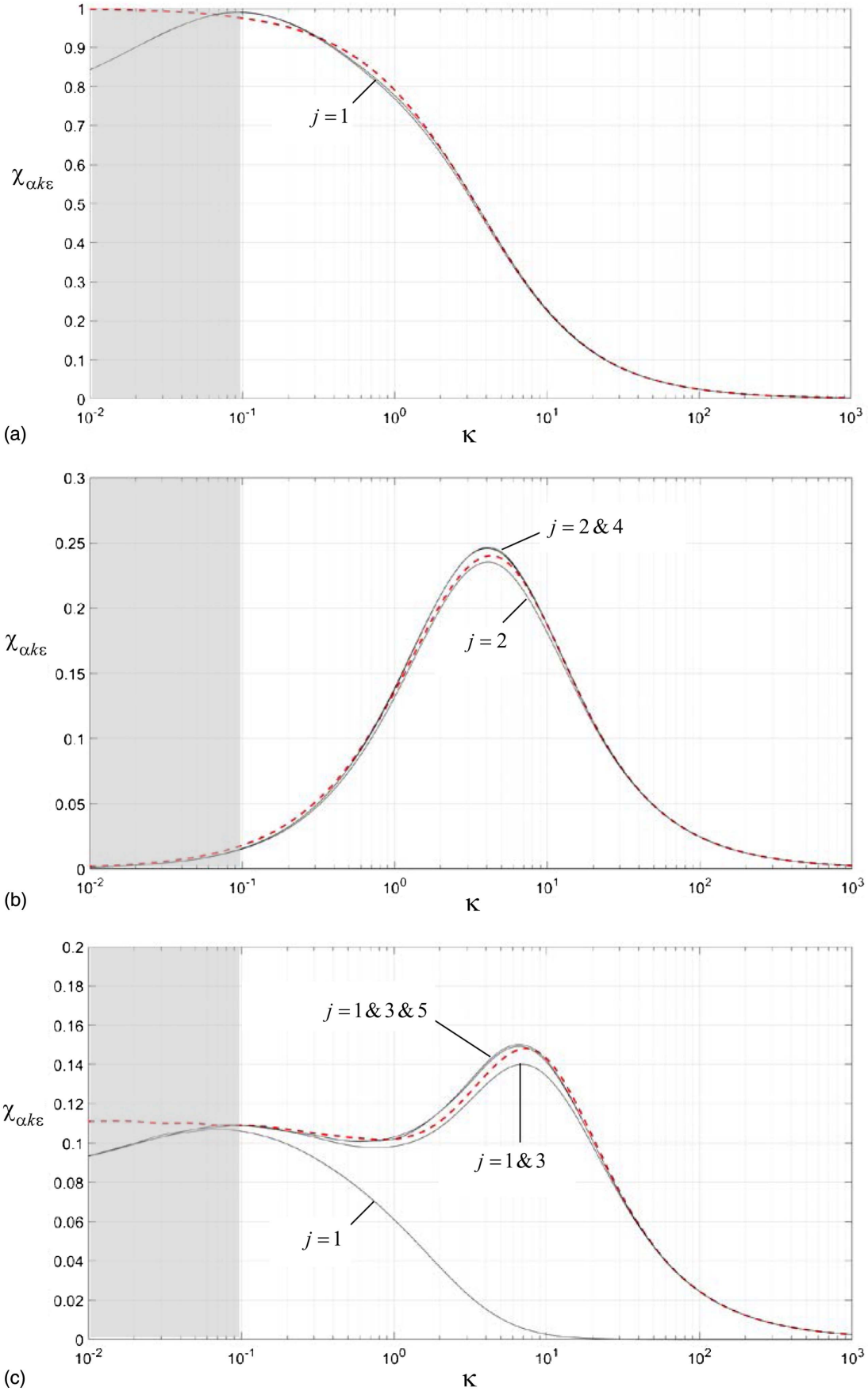

Fig. 3. Aerodynamic admittance for structure mode in Eq. (24), series expansion of wind modes (solid line), and exact solution (dashed line): (a) $i = 1$; (b) $i = 2$; and (c) $i = 3$.

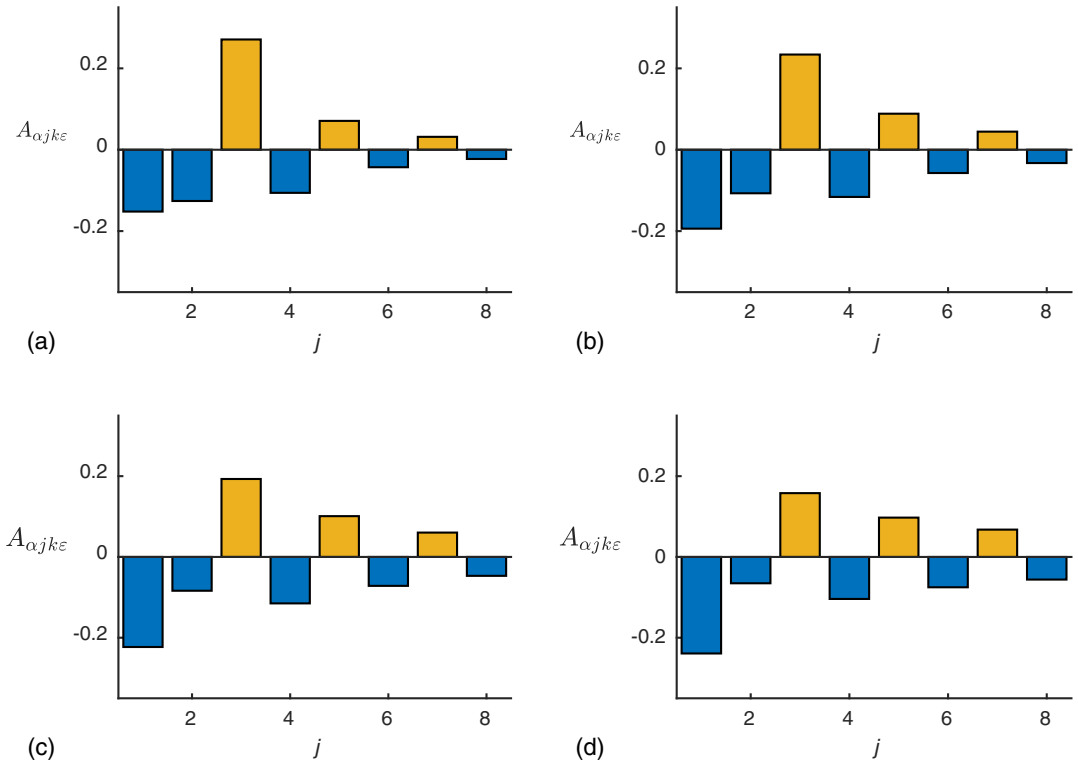

Fig. 4. Cross-modal participation coefficients for structure mode in Eq. (25) ($j = 1, 2, \ldots, 8$) for (a) $\kappa = 1$; (b) $\kappa = 5$; (c) $\kappa = 15$; and (d) $\kappa = 50$.

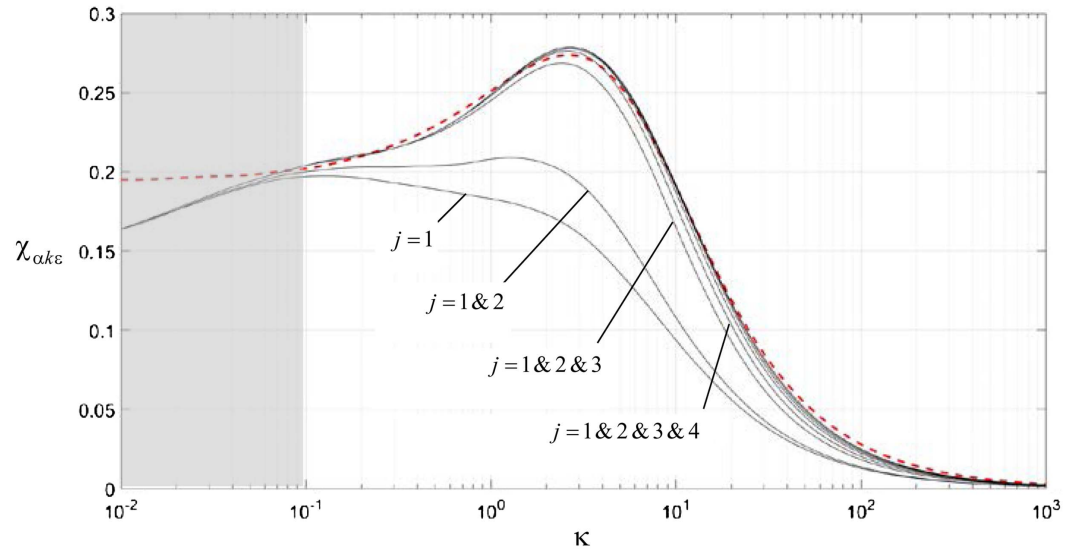

Fig. 5. Aerodynamic admittance for structure mode in Eq. (25): series expansion of wind modes (solid lines) and exact solution (dashed line).

have similar values when the reduced frequency varies. This makes it difficult to exclude a priori the contribution of any wind mode.

Fig. 5 shows the aerodynamic admittance $\chi_{\alpha k\varepsilon}$. Solid lines denote its reconstruction by the series expansion of wind modes expressed in closed form. The dashed line denote the rigorous formula of $\chi_{\alpha k\varepsilon}$. The wind mode with $j = 1$ is enough to reconstruct $\chi_{\alpha k\varepsilon}$ in the low-frequency range. On the other hand, in the frequency domain centered around κ_m, at least three or four wind modes are necessary to reconstruct $\chi_{\alpha k\varepsilon}$. In any case, in this unfavorable situation, a limited number of wind modes also is enough to reconstruct $\chi_{\alpha k\varepsilon}$.

Interpretations and Preliminary Expressions

Consider the structural mode defined by Eq. (24). Solid circles in Fig. 6 indicate the reduced frequency $\kappa = \kappa_m$ for which aerodynamic admittance attains its maximum value as a function of the subintervals $N = i$ in which structural and wind modes have constant sign for $j = i$. Crosses indicate the reduced frequencies for which reduced wind eigenvalues $\tilde{\gamma}_{j\varepsilon}$ attain their maximum value [Fig. 1(a)]. Because $\chi_{\alpha k\varepsilon}$ and $\tilde{\gamma}_{j\varepsilon}$ are flattened functions around their relative maxima, the agreement exhibited by Fig. 6 is excellent, as is the correspondence with the empirical formula proposed by Davenport (1977)

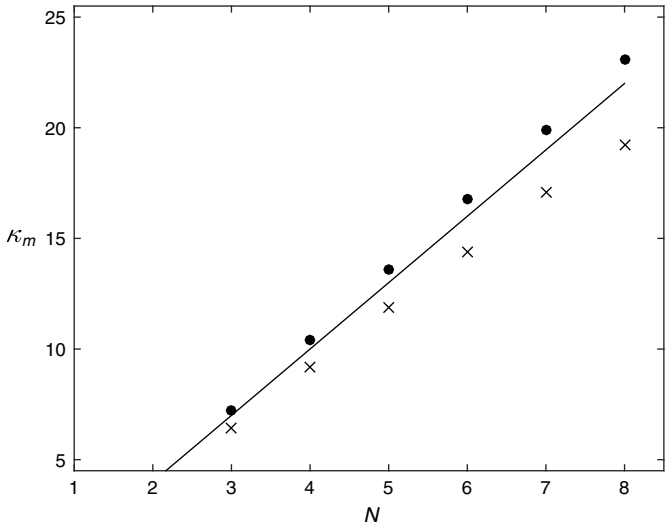

Fig. 6. Reduced frequency at which aerodynamic admittance (solid circles) and reduced wind eigenvalue (crosses) attain their relative maximum. The solid line refers to Eq. (26).

$$\kappa_m = 3N - 2 (N \geq 2) \tag{26}$$

This supports the interpretation according to which gust buffeting and aerodynamic admittance are strengthened with reference to the wind mode with the same wavelength of the structural mode. In terms of eigenvalues, this corresponds to the maximum power content of the turbulence coherent structures the reduced frequency of which is identified with the diameter of the eddies responsible of the maximum loading; in the framework of energy cascade, this diameter is proportional to $\bar{u}/n = c_\varepsilon l/\kappa_m$ [Eq. (11)]. In terms of eigenfunctions, they cause the maximum loading and response when eddies are in phase on structural portions in which structural modes have the same sign, and counterphase on structural portions in which structural modes have opposite sign.

Eq. (26), obtained for sinusoidal structural modes, offers a reasonable approximation for the κ_m values of nonsinusoidal modes. According to Fig. 2 of Solari and Martín (2020), the κ_m values for Modes 6–9, 13, and 14, united by $N = 2$, are similar to each other.

For sinusoidal structural modes, solid circles in Fig. 7 indicate the maxima $\chi_{\max}$ of aerodynamic admittance [Eq. (9)], and crosses indicate the maxima of the reduced wind eigenvalues [Fig. 1(a)]. The latter underestimate the former because they correspond to one single term of the sum in Eq. (23). The solid line corresponds to the empirical formula

$$\chi_{\max} = \frac{1}{2.5N - 1} \quad (N \geq 2) \tag{27}$$

according to which $\chi_{\max}$ decreases as N increases. Hollow circles in Fig. 7 indicate χ_0 for odd k values, and the dashed line derives from substituting Eq. (24) into Eq. (13); this provides

$$\chi_0 = \frac{1}{N^2} \quad (N \geq 1) \tag{28}$$

In contrast to Eq. (26), Fig. 7 indicates that the spread of $\chi_{\max}$ for nonsinusoidal structural modes is quite large. This is confirmed by Fig. 2 of Solari and Martín (2020), in which $\chi_{\max}$ for Modes 6–9, 13, and 14, united by $N = 2$, varies from 0.191 to 0.333.

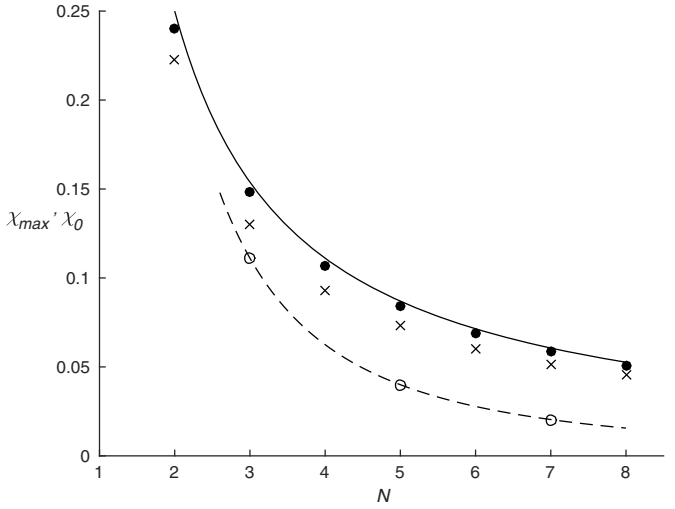

Fig. 7. Relative maxima of aerodynamic admittance (solid circles) and reduced wind eigenvalues (crosses). Solid line refers to Eq. (27), and hollow circles and dashed line refer to χ_0.

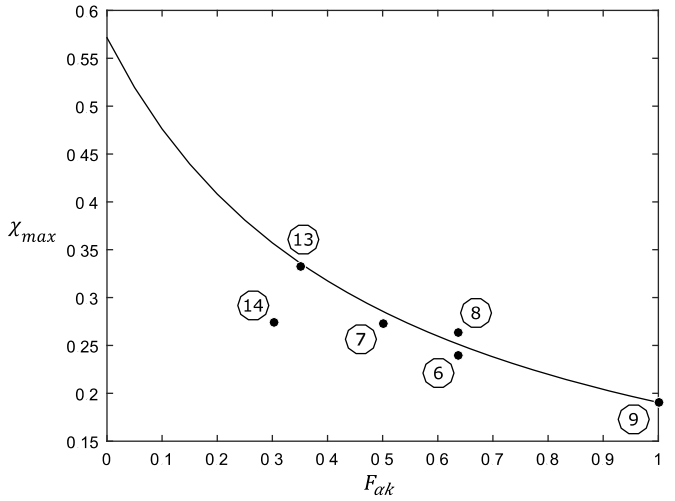

Fig. 8. Relative maxima of the aerodynamic admittance (solid circles) for nonsinusoidal modes with $N = 2$. The solid line refers to Eq. (29).

To clarify this aspect, solid circles in Fig. 8 show $\chi_{\max}$ (for Modes 6–9, 13, and 14) as a function of $F_{\alpha k}$ [Eq. (10)]; the solid line corresponds to the preliminary empirical formula

$$\chi_{\max} = \frac{1}{3.5F_{\alpha k} + 1.75} \quad (N = 2) \tag{29}$$

according to which $\chi_{\alpha k \varepsilon}$ decreases as $F_{\alpha k}$ increases. Mode 14 has anomalous properties.

Finally, the different trends of Eqs. (27) and (28) due to the fact, previously noted, that the aerodynamic admittance of the Type C intermediate modes involves the contribution of two wind modes, the first mode with a low-frequency content and the $j = i$th mode with a high-frequency content. The χ_0 values for Modes 13 and 14 ($N = 2$) in Fig. 2 of Solari and Martín (2020) confirm that $\chi_{\alpha k \varepsilon}$ decreases as $F_{\alpha k}$ increases.

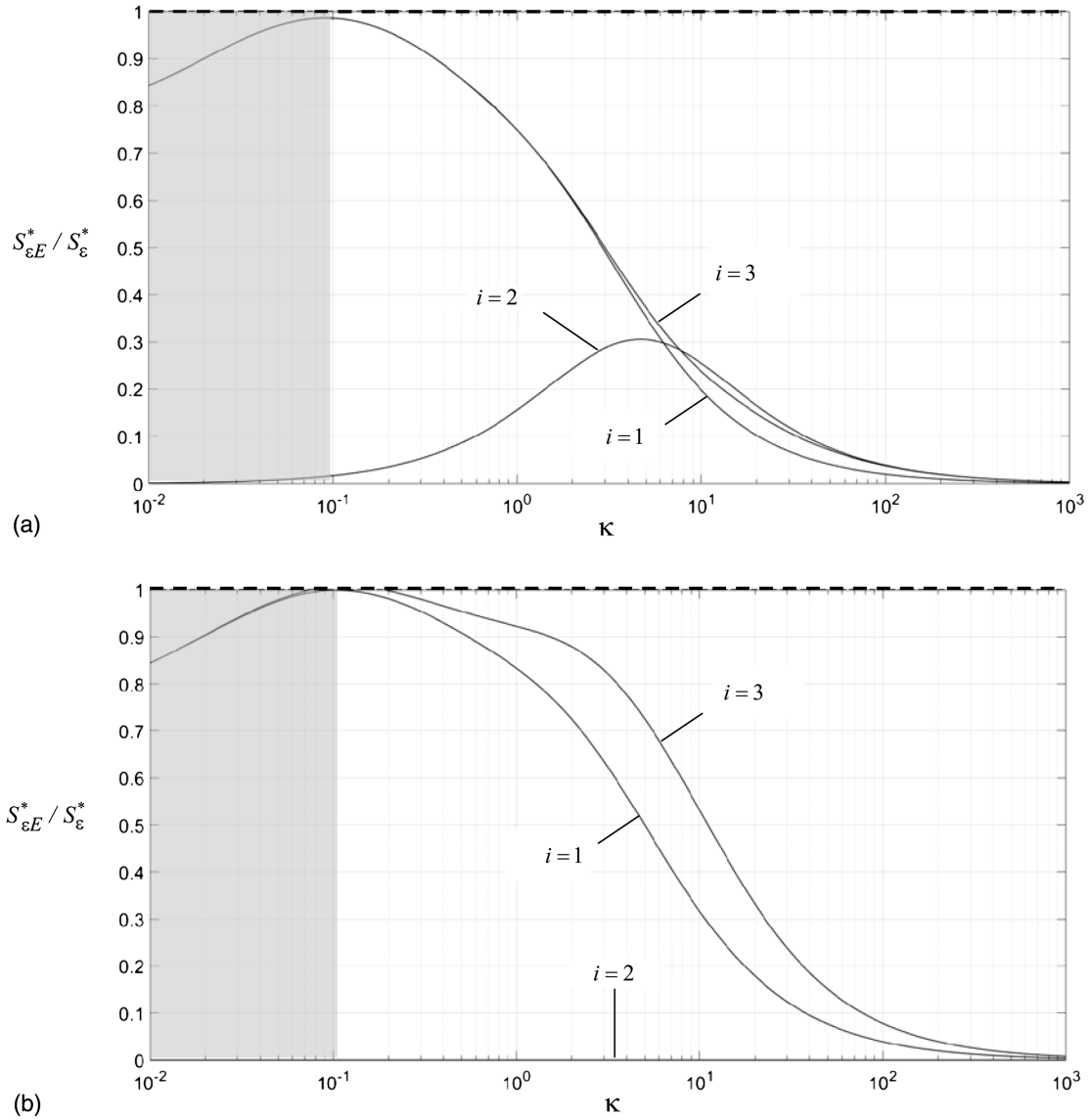

Fig. 9. $S^*_{\varepsilon E}/S^*_{\varepsilon}$ for the structural mode in Eq. (24) with $i = 1, 2, 3$ (solid lines) and its reference unit value (dashed line): (a) $\zeta = 0.25$; and (b) $\zeta = 0.5$.

Effective Turbulence

With the rigorous expression of $\chi_{\alpha k\varepsilon}$ [Eq. (9)] known, the evaluation of aerodynamic admittance through a series of wind modes [Eq. (23)] makes it possible to recognize which wind modes are necessary to reconstruct this function and thus to supply its physical interpretation. From this point of view, analyses carried out in previous sections are exhaustive. Effective turbulence (Tubino and Solari 2007) contributes to clarifying this issue further.

Effective turbulence is defined as the turbulence reconstructed taking into account the wind modes capable of effectively reproducing a given quantity, in this case aerodynamic admittance. Invoking Eqs. (18), (20), and (22), effective turbulence is characterized here by the PSD and coherence function

$$S^*_{\varepsilon E}(\zeta, n) = S^*_{\varepsilon}(\bar{\zeta}; n) \sum_{j=E} \theta^2_{j\varepsilon}(\zeta, n) \tilde{\gamma}_{j\varepsilon}(n) \tag{30}$$

$$\mathrm{Coh}_{\varepsilon\varepsilon E}(\zeta, \zeta'; n) = \sum_{j=E} \theta_{j\varepsilon}(\zeta, n) \theta_{j\varepsilon}(\zeta', n) \tilde{\gamma}_{j\varepsilon}(n) \tag{31}$$

where $j = E$ denotes a sum over the sole effective wind modes, namely those modes necessary to reconstruct aerodynamic admittance with reasonable approximation.

Sinusoidal Structural Modes

Fig. 9 shows $S^*_{\varepsilon E}/S^*_{\varepsilon}$ for the structural modes defined by Eq. (24) with $i = 1, 2, 3$ (solid lines). For $i = 1$, $j = 1$; for $i = 2$, $j = 2$; for $i = 3$, $j = 1$ and 3. The dashed lines indicate the sum over j extended to all wind modes. Fig. 9(a) refers to $\zeta = 0.25$, and Fig. 9(b) refers to $\zeta = 0.5$. The harmonic content of effective turbulence for $i = 2$ is null for $\zeta = 0.5$, i.e., the position in which the second wind mode is null. Furthermore, $S^*_{\varepsilon E}/S^*_{\varepsilon}$ is localized around the harmonic content of the effective reduced eigenvalues, and it always is smaller than one; this confirms that the power content of effective turbulence is reduced drastically compared with that of real turbulence.

Fig. 10 shows $\mathrm{Coh}_{\varepsilon\varepsilon E}$ [Eq. (31)] for the structural modes defined by Eq. (24) with $i = 1, 2, 3$ (solid lines), evaluated as for Fig. 9. Dashed lines indicate the sum over j extended to all wind modes. Figs. 10(a and b) refer to $\zeta = 0.25$ and $\zeta' = 0.5$, and $\zeta = 0.25$ and

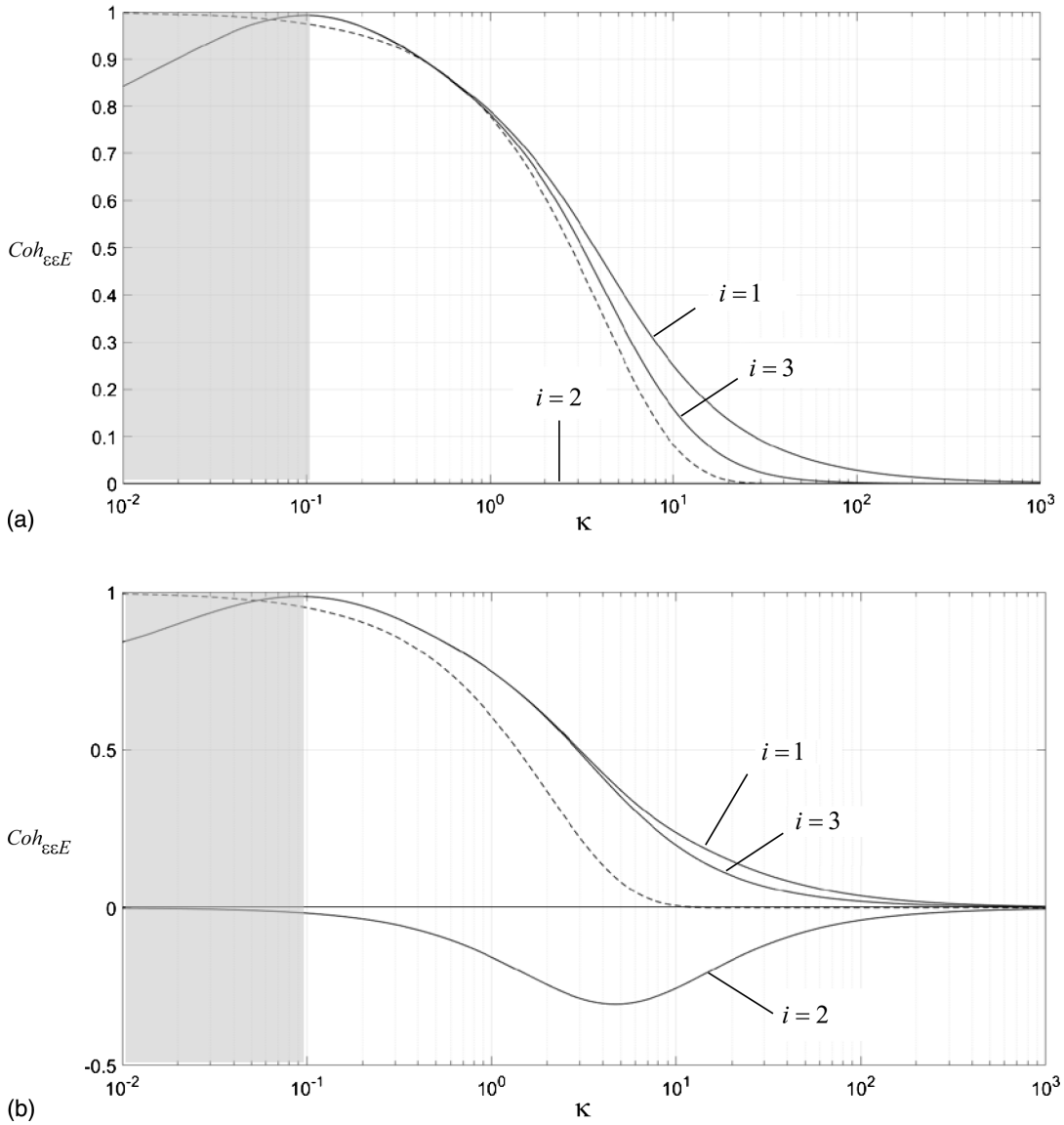

Fig. 10. $\mathrm{Coh}_{\varepsilon\varepsilon E}$ for the structural mode in Eq. (24) with $i = 1, 2, 3$ (solid lines) and its reference value $\mathrm{Coh}_{\varepsilon\varepsilon}$ (dashed lines): (a) $\zeta = 0.25$ and $\zeta' = 0.5$; and (b) $\zeta = 0.25$ and $\zeta' = 0.75$.

$\zeta' = 0.75$, respectively. For structural modes with $i = 1, 3$, $\mathrm{Coh}_{\varepsilon\varepsilon E}$ always is greater than $\mathrm{Coh}_{\varepsilon\varepsilon}$ because it involves a limited number of coherent wind modes. The situation is different for $i = 2$: with fixed $\zeta = 0.25$, $\mathrm{Coh}_{\varepsilon\varepsilon E} = 0$ for $\zeta' = 0.50$, i.e., the position where the second wind mode is null; instead, $\mathrm{Coh}_{\varepsilon\varepsilon E} < 0$ for $\zeta' = 0.75$ because the wind loading is counterphase for $\zeta < 0.5$ and $\zeta > 0.5$, where the eigenfunction of the second wind mode changes its sign.

Structural Mode 14

Adopting the same representation of Figs. 9 and 10, Figs. 11 and 12 show the diagrams of $S^*_{\varepsilon E}/S^*_{\varepsilon}$ and $\mathrm{Coh}_{\varepsilon\varepsilon E}$ for the structural mode defined by Eq. (25). As proved previously, the effective turbulence takes into account at least the first four wind modes.

Solid lines in Fig. 11 show $S^*_{\varepsilon E}/S^*_{\varepsilon}$ for different ζ values; the diagrams almost perfectly overlap. The dashed line indicates the sum over j extended to all wind modes. The effective turbulence PSD mostly is eroded in the high frequency range.

Solid lines in Figs. 12(a and b) show $\mathrm{Coh}_{\varepsilon\varepsilon E}$ for $\zeta = 0.25$ and $\zeta' = 0.5$, and $\zeta = 0.25$ and $\zeta' = 0.75$. Dashed lines indicate the sum over j extended to all wind modes. In this situation, effective coherence is close to the real coherence. However, reconstructing $\mathrm{Coh}_{\varepsilon\varepsilon E}$ for $\zeta = 0.25$ and $\zeta' = 0.75$ by four wind modes leads to slightly negative values in the high-frequency range. This shortcoming may be overcome by making recourse to more wind modes.

PSD Inequality Chain

The PSDs of real, effective and equivalent turbulence are linked by the chain of inequalities

$$S^*_{\varepsilon,eq}(n) \le S^*_{\varepsilon E}(\bar{\zeta}, n) \le S^*_{\varepsilon}(\bar{\zeta}, n) \tag{32}$$

Here, $S^*_{\varepsilon E} < S^*_{\varepsilon}$ or $S^*_{\varepsilon E} = S^*_{\varepsilon}$ depends on whether the sum in Eq. (30) is extended to a subset or a full set of wind modes; $S^*_{\varepsilon,eq} \le S^*_{\varepsilon}$ derives from Eq. (8) because $\chi_{\alpha k\varepsilon} \le 1$ [Eq. (9)]; $S^*_{\varepsilon,eq} \le S^*_{\varepsilon E}$ is more subtle: whereas the effective turbulence field that reconstructs the actual wind loading is partially coherent [Eqs. (30) and (31)], the equivalent turbulence field, identified by $S^*_{\varepsilon,eq}$, is identically coherent, so it includes the effect of coherence function (less than or equal to 1).

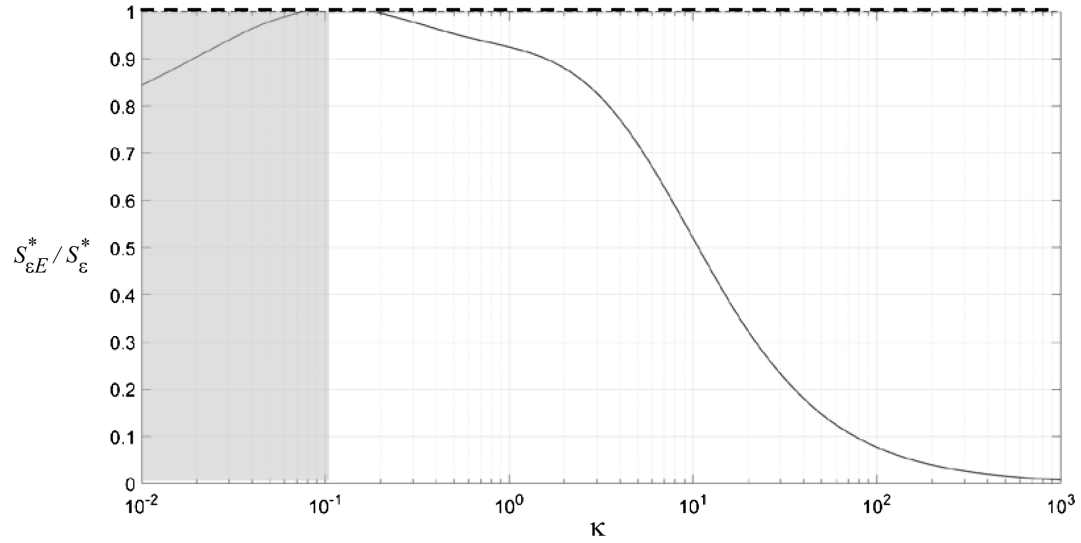

Fig. 11. $S^*_{\varepsilon E}/S^*_{\varepsilon}$ for the structural mode in Eq. (25) (solid line) and its reference unit value (dashed line): $\zeta = 0.25$ and 0.50.

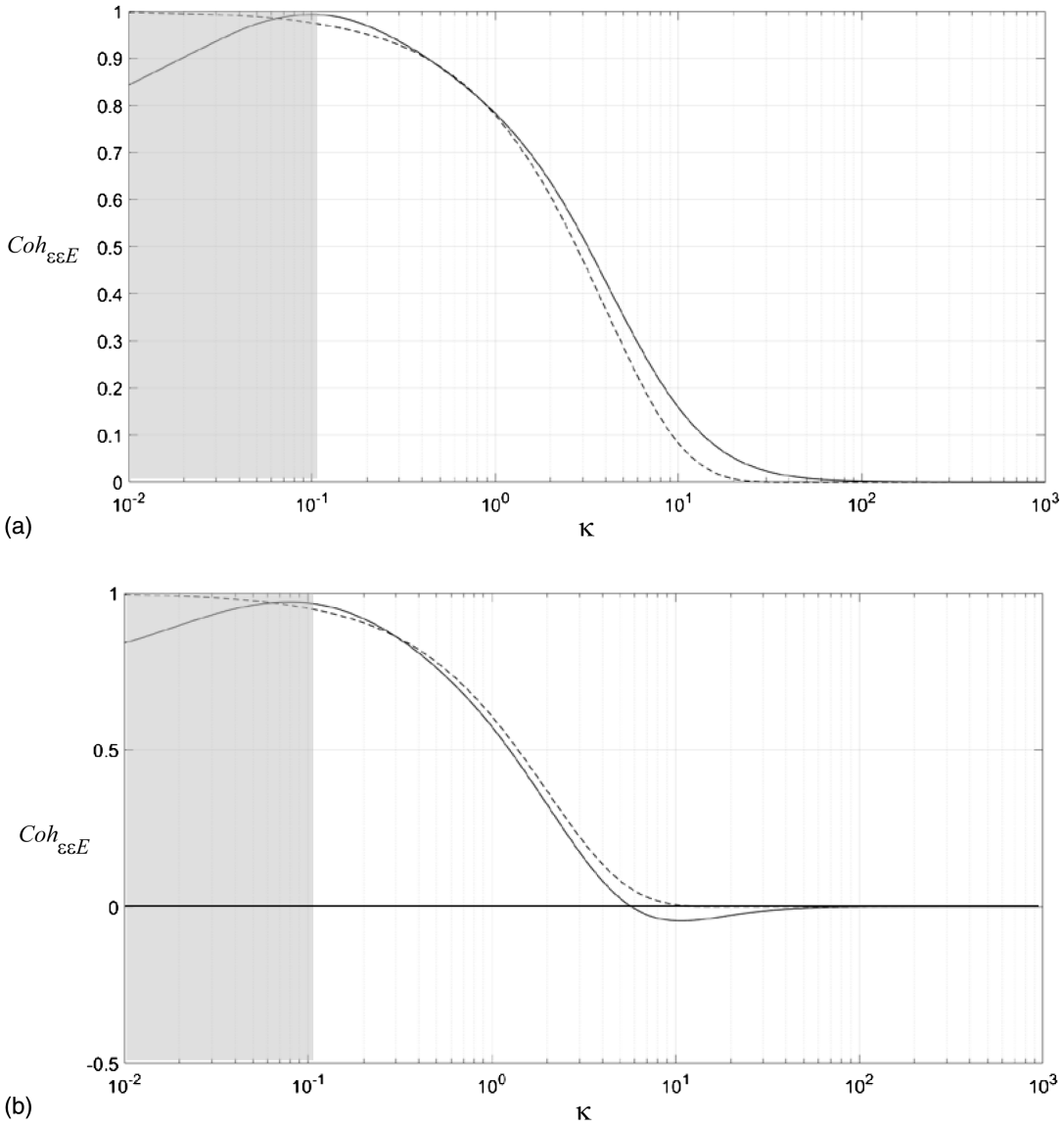

Fig. 12. $\mathrm{Coh}_{\varepsilon\varepsilon E}$ for the structural mode in Eq. (25) (solid line) and its reference value $\mathrm{Coh}_{\varepsilon\varepsilon}$ (dashed lines): (a) $\zeta = 0.25$ and $\zeta' = 0.5$; and (b) $\zeta = 0.25$ and $\zeta' = 0.75$.

In reality, the ideal situation outlined by Eq. (32) may be violated in specific frequency ranges if wind modes or aerodynamic admittance are expressed by approximate solutions, or if the sum in Eq. (30) retains an insufficient number of wind modes.

Closed-Form Solution

Focusing on Type A regular modes, Piccardo and Solari (1998) provided a simple and precise CFS of $\chi_{\alpha k\varepsilon}$. For Type B and C modes, Solari and Martín (2020) developed a CFS that consists of dividing the structural domain into subdomains in which piecewise structural modes are regular and do not change sign. This made it possible to derive a solution based on the application of classical methods to each subdomain. This solution is precise and simple for modes with a few changes of sign, but becomes laborious with increasing mode complexity.

Accordingly, a new CFS was developed here, which is easier and more straightforward, and consists of expressing aerodynamic admittance by an empirical formula that (1) reproduces its shape qualitatively; (2) satisfies Eq. (13) for $n = 0$; (3) has a relative maximum $\chi_{\max}$ for $\kappa = \kappa_m$; and (4) matches the trend of Eq. (14) for n tending to infinity. A preliminary expression that fulfils Points 1, 2, and 4 rigorously and Point 3 approximately is given by (Fig. 13)

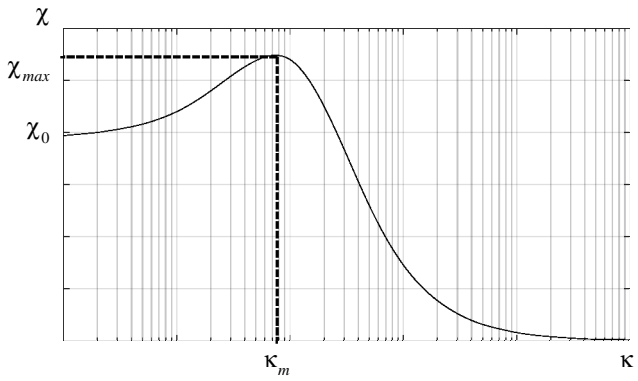

Fig. 13. Qualitative diagram of $\chi = \chi_{\alpha k\varepsilon}(n)$ as a function of $\kappa = \kappa_{\alpha k\varepsilon}$.

$$\chi_{\alpha k\varepsilon}(n) = \frac{\left(a + \frac{\kappa}{\kappa_m}\right)}{\sqrt{b^2\left(1 - \frac{\kappa^2}{\kappa_m^2}\right)^2 + 4c^2\frac{\kappa^2}{\kappa_m^2}}} \tag{33}$$

$$\begin{aligned} a &= \chi_0\kappa_m k^* \\ b &= \kappa_m k^* \\ c &= \frac{1 + \chi_0\kappa_m k^*}{2\chi_{\max}} \end{aligned} \tag{34}$$

where χ_0 is given by Eq. (13); κ_m is given by Eq. (26); $\chi_{\max}$ is given by Eq. (27) or Eq. (29); and $k^* = k^*_{\alpha k}$ is given by Eq. (14). Table 1 compares the rigorous and approximate values of these parameters. A better agreement probably is possible through more-refined analyses.

Fig. 14 compares the rigorous expressions of $\chi_{\alpha k\varepsilon}$ given by Eq. (9) for Modes 6, 10, 14, and 15 (solid lines) with Eq. (33) applied to both the rigorous (dashed lines) and approximate (dashed-dotted lines) $\chi_0, \kappa_m, \chi_{\max}$, and k^* values. This figure and other diagrams not reported here show that this method always produces excellent approximations for Type B modes, whereas it is less accurate for Type C modes. The estimation of the approximate parameters of Eq. (33) is coarse, especially for Mode 14, which once again is the most complex to interpret and analyze.

In conclusion, deriving analytical expressions of the aerodynamic admittance for arbitrary modes, independently of the method applied and the precision attained, is a secondary result with respect to the physical interpretation of this issue. At present, numerical analysis generally is better than using simplified formulas. However, such formulas explain the explicit dependence of aerodynamic admittance on its parameters.

Applications

To determine the efficacy of the aforementioned methods, the two structural test cases previously analyzed by Solari and Martín (2020) were studied: (1) a pedestrian footbridge (Type B, Mode 6); and (2) a steel chimney constrained to a nearby building (Type C, Mode 14). The 10-min mean wind speed had a logarithmic profile, and the turbulent field was modeled by Eqs. (4), (6), and (7). Their dynamic response was evaluated as described by

Table 1. Rigorous and approximate values of model parameters in Eq. (33)

Mode type	Mode No.	χ_0 [Eq. (13)]	k^* [Eq. (14)]	Rigorous parameters Fig. 2 (Solari and Martín 2020)		Approximate parameters Eqs. (26) and (27) or Eq. (29)	
				κ_m	$\chi_{\max}$	κ_m	$\chi_{\max}$
B	6	0	0.405	4.22	0.240	4.00	0.250
	7	0	0.375	3.40	0.273	4.00	0.286
	8	0	0.405	3.48	0.263	4.00	0.251
	9	0	0.500	3.80	0.191	4.00	0.190
	10	0	0.405	10.43	0.107	10.00	0.111
	11	0	0.405	16.76	0.069	16.00	0.071
	12	0	0.405	23.06	0.051	22.00	0.053
C	13	0.179	0.321	2.79	0.333	4.00	0.336
	14	0.194	0.344	2.60	0.274	4.00	0.356
	15	0.111	0.405	7.24	0.148	7.00	0.154
	16	0.040	0.405	13.60	0.084	13.00	0.087
	17	0.020	0.405	19.91	0.059	19.00	0.061

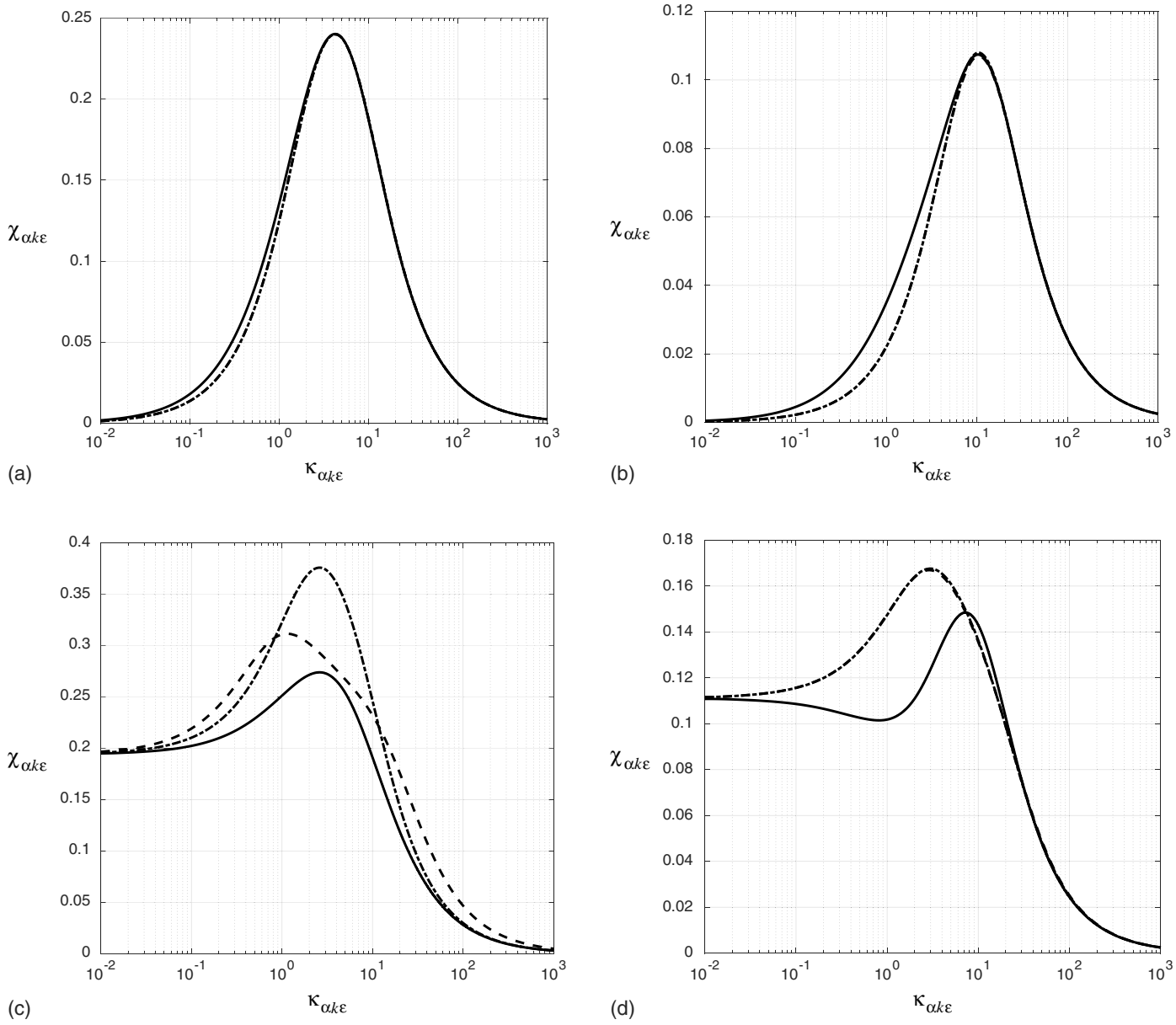

Fig. 14. Rigorous diagrams of $\chi_{\alpha k\varepsilon}$ [Eq. (9), solid lines] and Eq. (33) evaluated for the rigorous (dashed lines) and approximate (dash-dotted lines) $\chi_0, \kappa_m, \chi_{\max}$, and k^* values (Table 1): (a) Modes 6; (b) Mode 10; (c) Mode 14; and (d) Mode 15 in Solari and Martín (2020).

Solari and Martín (2020), determining aerodynamic admittance by the rigorous Eq. (9) and the closed-form Eq. (33) based on using the approximate values of model parameters (Table 1).

Structure 1—Pedestrian Footbridge

The crosswind fluctuating load in the vertical direction y was due to the longitudinal and vertical turbulence components, u' and w'. Fig. 15 shows the aerodynamic admittances and the PSD of the modal force. Solid lines indicate the rigorous solution, and dashed lines indicate the CFS, where $k^* = 0.405$ [Eq. (14)], $F_{\alpha k} = 2/\pi$ [Eq. (10)], $\kappa_m = 4.00$ [Eq. (26)], $\chi_0 = 0$ [Eq. (13)], and $\chi_{\max} = 0.25$ [Eq. (27)]. Aerodynamic admittances were null at the zero frequency, and their relative maximum was well below unity. The modal force was due mainly to longitudinal turbulence.

Table 2 lists the main parameters of the vertical displacement for $z = l/4$ due to the first vertical Mode 6, evaluated by the rigorous and approximate solutions. Similar to the method derived by Solari and Martín (2020), the CFS gave almost exact results. The background response was small, and the resonant response prevailed regardless of structural flexibility.

Structure 2—Steel Chimney

The alongwind fluctuating load was due to the longitudinal turbulence. Fig. 16 shows the aerodynamic admittance and the PSD of the modal force. Solid lines indicate the rigorous solution, and dashed lines indicate the CFS, where $k^* = 0.344$ [Eq. (14)], $F_{\alpha k} = 0.3026$ [Eq. (10)], $\kappa_m = 4.00$ [Eq. (26)], $\chi_0 = 0.194$ [Eq. (13)], and $\chi_{\max} = 0.356$ [Eq. (29)]. The aerodynamic admittance remained well below unity, eroding quite uniformly the harmonic content of the modal force. The CFS was quite coarse due to the coarse estimation of $\chi_{\max}$ (Table 1).

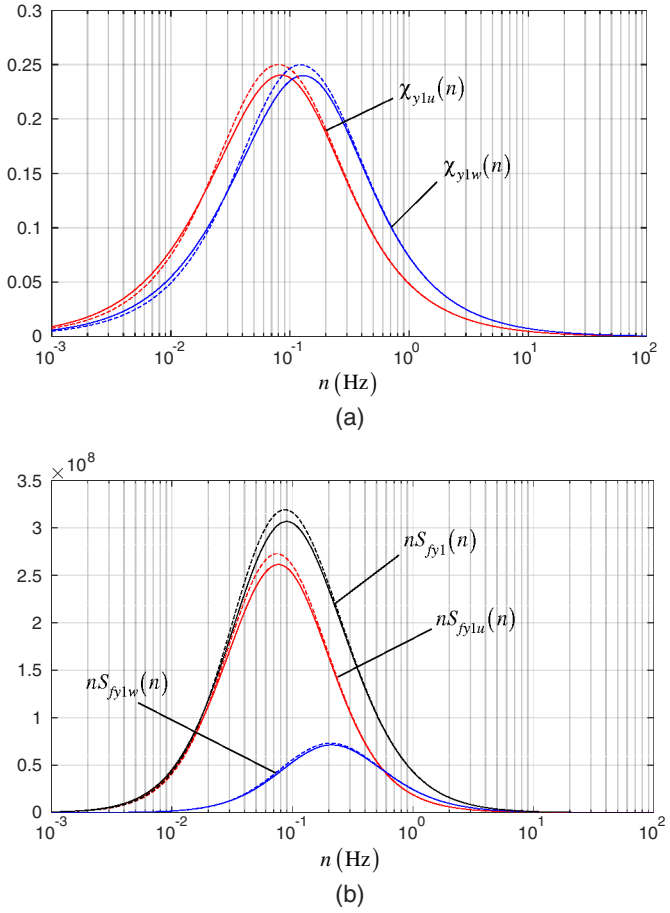

Fig. 15. Pedestrian footbridge: (a) aerodynamic admittances; and (b) PSD of the modal force.

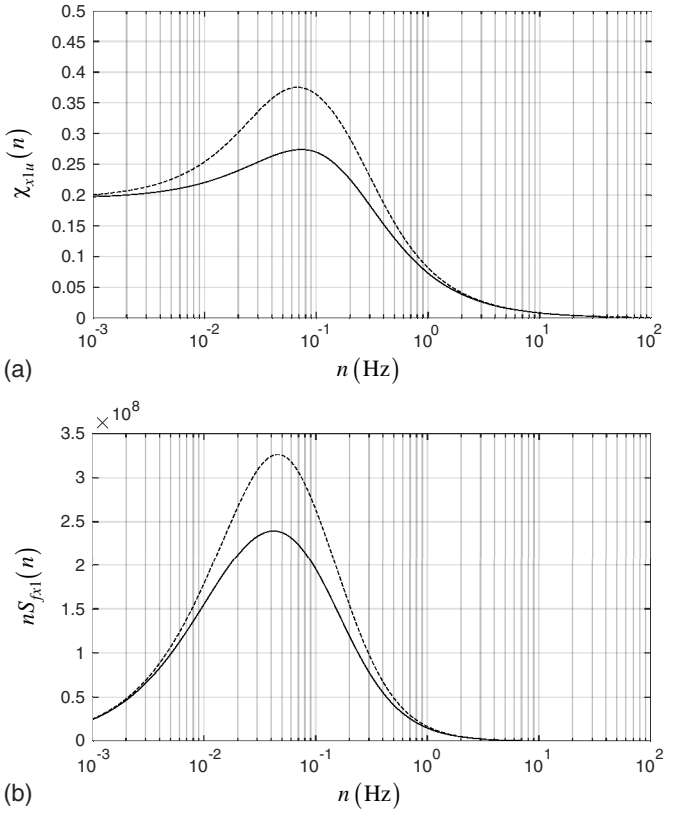

Fig. 16. Steel chimney: (a) aerodynamic admittance; and (b) PSD of the modal force.

Table 3 lists the main parameters of the alongwind displacement for $z = l$ due to the first longitudinal Mode 14, evaluated by the rigorous and approximate solutions. The errors due to the latter were greater than those provided by the CFS in Solari and Martín (2020) due to the coarse estimation of $\chi_{\max}$ (Table 1) and the limited quality of Eqs. (27) and (29) for Type C modes. These aspects involve ample room for improvement.

Conclusions and Prospects

This paper and its companion addressed the role of the modal shape on the aerodynamic admittance of structures. Analyses were restricted to slender structures and single modes, applied quasi-steady theory, and neglected the imaginary part of the turbulence cross-spectrum.

Solari and Martín (2020) studied the properties of aerodynamic admittance and derived this quantity in closed form for any mode. This solution is precise and simple for modes with a few changes of sign, but becomes laborious with increasing mode shape complexity; in addition, invoking the sole principles of energy cascade, it provides a limited advance of the physical interpretation of the relationship linking aerodynamic admittance with modal shape, which inspired this research. The present paper overcame these limits through the application of proper orthogonal decomposition.

Addressing the problem in this novel framework, POD was applied with the aim of expanding the turbulence field into a series of eigenfunctions, the wind modes, which are perfectly coherent along the structural axis and perfectly incoherent with each other. They are weighted by independent time histories the spectral content of which is defined by wind eigenvalues. The change of sign of wind modes corresponds to counterphase turbulence coherent structures that energy cascade alone cannot interpret.

Introducing this series expansion into the modal force gives rise to a pillar of double modal transformation, cross-modal participation coefficients, which quantify the influence of each wind mode

Table 2. Displacement parameters of Structure 1 for $z = l/4$

Parameter	Displacement parameter	Rigorous	Approximate	Error (%)
$\bar{y}$ (m)	Mean value	-0.4823×10^{-4}	-0.4823×10^{-4}	—
σ_{By1} (m)	Standard deviation of background part	0.2484×10^{-4}	0.2513×10^{-4}	+1
σ_{Ry1} (m)	Standard deviation of resonant part	0.1071×10^{-3}	0.1073×10^{-3}	—
σ_y (m)	Standard deviation	0.1099×10^{-3}	0.1102×10^{-3}	—
ν_y (Hz)	Expected frequency	1.196	1.195	—
g_y	Peak coefficient	3.785	3.785	—
$\bar{y}_{\max}$ (m)	Maximum value	0.4642×10^{-3}	0.4653×10^{-3}	—

Table 3. Displacement parameters of Structure 2 for $z = l$

Parameter	Displacement parameter	Rigorous	Approximate	Error (%)
$\bar{x}$ (m)	Mean value	−0.00323	−0.00323	—
σ_{Bx1} (m)	Standard deviation of background part	0.00225	0.00251	+11
σ_{Rx1} (m)	Standard deviation of resonant part	0.00495	0.00538	+9
σ_x (m)	Standard deviation	0.00544	0.00594	+9
ν_x (Hz)	Expected frequency	0.510	0.507	−1
g_x	Peak coefficient	3.554	3.552	—
$\bar{x}_{\max}$ (m)	Maximum value	0.0226	0.0243	+7

on the structure mode for which aerodynamic admittance is evaluated. The expansion of aerodynamic admittance into a series of wind modes further clarifies its different behavior with regard to Type A, B, and C modes.

Type A modes with constant sign mainly are excited by the first wind mode whose reduced eigenvalue decreases when the reduced frequency increases. This gives rise to the classical decrease of aerodynamic admittance that energy cascade thoroughly interprets.

Type B skew-symmetric modes are excited mainly by wind modes with the same wavelength. Thus, aerodynamic admittance mostly reproduces the shape of its reduced eigenvalue which is null at the zero frequency, increases to a relative maximum, and then tends to zero.

Type C intermediate modes are excited mainly by two wind modes: the first mode and the mode with the same wavelength. The former gives rise to a nonnull value of aerodynamic admittance at the zero frequency, and the second is responsible of the relative maximum that occurs for the maximum power of this wind mode.

Joining Type B and C modes under the common label of modes that change sign, these remarks support the interpretation that gust buffeting and aerodynamic admittance are strengthened in relation to wind modes or waves corresponding to coherent structures associated with eddies the diameter of which corresponds to the maximum power of the reduced wind eigenvalue.

The recourse to effective turbulence, namely the turbulence field reconstructed by taking into account the wind modes capable of reproducing aerodynamic admittance, further clarifies this issue. Its harmonic content admits an upper bound related to the harmonic content of the actual turbulence and a lower bound related to the harmonic content of the equivalent turbulence defined by the enhanced equivalent spectrum technique (Solari and Martín 2020).

Finally, this paper proposes a simple and preliminary closed-form expression of the aerodynamic admittance of structures with arbitrary modes which matches the ensemble of the preceding concepts and principles, stressing the role of the parameters on which this function depends.

The prospects of this research seem to be wide, and mostly are oriented along two main directions.

The first direction continues the present analyses. The authors are aware that wind-sensitive structures with complex modes are candidates for numerical analysis. Equally, the authors believe that the analytical study of the aerodynamic admittance related to a single mode is a first step toward physical and engineering interpretations currently missing or incomplete, as well as more-extensive and complex evaluations that take into account the interaction of different modes in the resonant field and the role of arbitrary influence functions in the background domain; the second argument especially can benefit greatly from the results of the present study.

The second direction does not consider the following hypotheses used as the basis of the present study: the quasi-steady theory and neglecting the imaginary part of the turbulence cross-spectrum. The first topic calls for extensive wind tunnel tests and CFD simulations, which to a small extent already are available, based on fixing the structural properties, and therefore partially losing generality. The second calls for systematic field measurements currently missing in the literature.

Data Availability Statement

Data, models, or code that support the findings of this study are available from the corresponding author upon reasonable request.

Acknowledgments

The research activity carried out for this paper by the first author and partly for the second one is funded by the European Research Council (ERC) under the European Union's Horizon 2020 research and innovation program (Grant Agreement No. 741273) for the Project THUNDERR - Detection, simulation, modelling and loading of thunderstorm outflows to design wind-safer and cost-efficient structures, supported by an Advanced Grant (AdG) 2016.

References

Carassale, L., G. Piccardo, and G. Solari. 2001. "Double modal transformation and wind engineering applications." *J. Eng. Mech.* 127 (5): 432–439. https://doi.org/10.1061/(ASCE)0733-9399(2001)127:5(432).

Carassale, L., and G. Solari. 2002. "Wind modes for structural dynamics: A continuous approach." *Probab. Eng. Mech.* 17 (2): 157–166. https://doi.org/10.1016/S0266-8920(01)00036-4.

Carassale, L., G. Solari, and F. Tubino. 2007. "Proper orthogonal decomposition in wind engineering. Part 2: Theoretical aspects and some applications." *Wind Struct.* 10 (2): 177–208. https://doi.org/10.12989/was.2007.10.2.177.

Chen, X., and A. Kareem. 2005. "Proper orthogonal decomposition-based modeling, analysis, and simulation of dynamic wind load effects on structures." *J. Eng. Mech.* 131 (4): 325–339. https://doi.org/10.1061/(ASCE)0733-9399(2005)131:4(325).

Davenport, A. G. 1977. "The prediction of the response of structures by gusty wind." In *Safety of structures under dynamic loading*, edited by I. Holand, D. Mavlie, G. Moe, and R. Sigbjörnsson, 257–284. Trondheim, Norway: Tapir.

Di Paola, M. 1998. "Digital simulation of wind field velocity." *J. Wind Eng. Ind. Aerodyn.* 74–76 (Apr): 91–109. https://doi.org/10.1016/S0167-6105(98)00008-7.

ESDU (Engineering Sciences Data Unit). 1991. *Characteristics of atmospheric turbulence near the ground. Part III: Variations in space and time for strong winds (neutral atmosphere)*. ESDU Item 86010. London: ESDU.

Hansen, S. O., and S. Krenk. 1999. "Dynamic along-wind response of simple structures." *J. Wind Eng. Ind. Aerodyn.* 82 (1–3): 147–171. https://doi.org/10.1016/S0167-6105(98)00215-3.

Li, Y., and A. Kareem. 1995. "Stochastic decomposition and application to probabilistic dynamics." *J. Eng. Mech.* 121 (1): 162–174. https://doi.org/10.1061/(ASCE)0733-9399(1995)121:1(162).

Mann, J. 1994. "The spatial structure of neutral atmospheric surface-layer turbulence." *J. Fluid Mech.* 273: 141–168. https://doi.org/10.1017/S0022112094001886.

Piccardo, G., and G. Solari. 1998. "Generalized equivalent spectrum technique." *Wind Struct.* 1 (2): 161–174. https://doi.org/10.12989/was.1998.1.2.161.

Solari, G. 2019. *Wind science and engineering: Origins, developments, fundamentals and advancements*. Cham, Switzerland: Springer.

Solari, G., and L. Carassale. 2000. "Modal transformation tools in structural dynamics and wind engineering." *Wind Struct.* 3 (4): 221–241. https://doi.org/10.12989/was.2000.3.4.221.

Solari, G., L. Carassale, and F. Tubino. 2007. "Proper orthogonal decomposition in wind engineering. Part 1: A state-of-the-art and some prospects." *Wind Struct.* 10 (2): 153–176. https://doi.org/10.12989/was.2007.10.2.153.

Solari, G., and P. Martín. 2020. "Gust buffeting and aerodynamic admittance of structures with arbitrary mode shapes. I: Enhanced equivalent spectrum technique." *J. Eng. Mech.* 147 (1): 04020142. https://doi.org/10.1061/(ASCE)EM.1943-7889.0001872.

Solari, G., and G. Piccardo. 2001. "Probabilistic 3-D turbulence modeling for gust buffeting of structures." *Probab. Eng. Mech.* 16 (1): 73–86. https://doi.org/10.1016/S0266-8920(00)00010-2.

Tamura, Y., S. Suganuma, H. Kikuchi, and K. Hibi. 1999. "Proper orthogonal decomposition of random wind pressure field." *J. Fluids Struct.* 13 (7–8): 1069–1095. https://doi.org/10.1006/jfls.1999.0242.

Tubino, F., and G. Solari. 2007. "Gust buffeting of long span bridges: Double Modal Transformation and effective turbulence." *Eng. Struct.* 29 (8): 1698–1707. https://doi.org/10.1016/j.engstruct.2006.09.019.